High-Voltage Symmetric Supercapacitor Based on 2D Titanium Carbide (MXene, Ti_2CT_x)/Carbon Nanosphere Composites in a Neutral Aqueous Electrolyte

Sharona A. Melchior,[1,2,3] Kumar Raju,[4] Innocent S. Ike,[1,2,3,5] Rudolph M. Erasmus,[2,3,6] Guy Kabongo,[7] Iakovos Sigalas,[1,2,3] Sunny E. Iyuke,[1] and Kenneth I. Ozoemena[3,7,*,z]

[1]*School of Chemical and Metallurgical Engineering, University of the Witwatersrand, Johannesburg 2050, South Africa*
[2]*DST-NRF Centre of Excellence in Strong Materials (COE-SM), University of the Witwatersrand, Johannesburg 2050, South Africa*
[3]*Materials for Energy Research Group (MERG), University of the Witwatersrand, Johannesburg 2050, South Africa*
[4]*Materials Science and Manufacturing, Council for Scientific and Industrial Research (CSIR), Pretoria 0001, South Africa*
[5]*Department of Chemical Engineering, Federal University of Technology, Owerri, Nigeria*
[6]*Material Physics Research Institute, School of Physics, University of the Witwatersrand, Johannesburg 2050, South Africa*
[7]*Molecular Sciences Institute, School of Chemistry, University of the Witwatersrand, Johannesburg 2050, South Africa*

The energy storage performance of one of the lightest-known MXenes, Ti_2CT_x (MX) combined with carbon nanospheres (CNS) has been investigated as a symmetric electrode system in an aqueous electrolyte (1 M Li_2SO_4). The energy storage properties were interrogated using cyclic voltammetry (CV), galvanostatic cycling with potential limitation (GCPL), electrochemical impedance spectroscopy (EIS) and voltage-holding tests. The combined material (MX/CNS) demonstrated a higher specific capacity compared to each of the individual components. The material was fabricated with relatively high and low mass loadings, assembled into a symmetric device and performance compared. Specific capacitance, specific power and specific energy for the lower electrode mass loading of 180 $F{\cdot}g^{-1}$, 37.6 $kW{\cdot}kg^{-1}$ and 14.1 $W{\cdot}h{\cdot}kg^{-1}$ were all higher than 86 $F{\cdot}g^{-1}$, 20.1 $kW{\cdot}kg^{-1}$ and 6.7 $W{\cdot}h{\cdot}kg^{-1}$ for the higher mass loading. A wide voltage window of 1.5 V was obtained, but with limited long-term cycling behavior, suggesting the need for future improvement. Mathematical modelling and simulation of the supercapacitor showed good correlation with the experimental results, validating the model. The results reveal the potential of the Ti_2CT_x to be employed as a viable energy storage system for lightweight applications.

 [DOI: 10.1149/2.0401803jes]

Manuscript submitted November 20, 2017; revised manuscript received February 2, 2018. Published February 21, 2018.

As part of the increasing role of clean energy technologies, electrochemical capacitors (ECs) are continuously evolving components that contribute to meeting the demands of electronic apparatuses and systems and are projected to be even more significant in the future.[1] In 2011, Gogotsi and co-workers,[2] first synthesized a two-dimensional (2-D) layered material called MXene, by selectively etching aluminum (Al), using hydrofluoric acid (HF) from the MAX phase material. MAX phase materials are layered ternary carbide and nitride materials with the general chemical formula of $M_{n+1}AX_n$ (where 'M' represents an early transition metal, 'A' represents a group IIIA or IVA element, 'X' is C and/or N, and n may equal 1, 2, or 3). There are more than 70 different MAX phase compositions currently known.[3,4] MXenes are formed when the 'A' element is etched out of the MAX phase material, and subsequently have a general formula of $M_{n+1}X_nT_x$ (where T represent surface functional groups such as F, OH or O, and x is the number of functional groups that are attached to the surface following the etching process).[5] This newly discovered family of materials has similar properties to graphene with good electronic conductivity and different surface terminations enabling the possibility to manipulate their properties to fit different applications. 2-D materials potentially have large electroactive surfaces and therefore attract research attention. MXenes are currently studied, both theoretically and experimentally, as potential electrode materials for energy storage devices such as batteries[6–16] and ECs[9,14,17–32] as well as other uses.[33,34]

Although the MXene materials do not possess such a high surface area as electric double-layer capacitor (EDLC) materials,[6,11,24,35,36] they are suggested to employ the energy storage through pseudocapacitive ion intercalation route giving rise to high capacitance and attractive electrochemical properties without the need for a high surface area.[37] Ghidiu et al.[19] obtained excellent capacitance of 245 $F{\cdot}g^{-1}$ (900 $F{\cdot}cm^{-3}$) at 2 $mV{\cdot}s^{-1}$ in 1 M H_2SO_4 for $Ti_3C_2T_x$ films at a window of 0.55 V. The coulombic efficiency was close to 100% with no measurable capacitance losses even after 10,000 cycles. Lukatskaya et al.[38] indicated that the capacitance comes mainly from pseudocapacitive redox reactions of the Titanium. Gogotsi and co-workers[35,39] studied MXene as an anode material for Li-ion batteries (LiBs) and asymmetric cells and suggested the following lithiation and delithiation reactions taking place when Li^+ ions are inserted into the MXene matrix as described in Equation 1.

$$Ti_2CO_x + yLi^+ + ye^- \leftrightarrow Li_yTi_2CO_x \quad [1]$$

Ling et al.[23] and Zhao et al.[38] also showed that expanding the interlayer gaps improves the capacity by facilitating ion transport. MXene combined with nanocarbons[12,14,23,30,40,41] and polymers[17,23] were shown to yield better capacitance than pristine MXene but in a narrow voltage window (<1.0 V) in aqueous electrolytes[17,26,28–30,41] or higher voltage window (>1.0 V) in organic electrolyte.[14,40]

To date, nearly all reported works on MXene-based supercapacitors have been on the heavy MXene ($Ti_3C_2T_x$) rather than on the MXene type Ti_2CT_x, usually referred to as the lightest MXene.[24,35] It is known that the performance of the heavier MXene as a supercapacitor is higher than that of the lightest MXene. For example, in a recent work by Rakhi et al.,[25] the authors reported the specific capacitance of the symmetric $Ti_3C_2T_x$ as 79.9 $F{\cdot}g^{-1}$ which is about twice that of the Ti_2CT_x (32.3 $F{\cdot}g^{-1}$) obtained under the same experimental conditions (i.e., 30% wt KOH aqueous electrolyte, at a maximum voltage of 0.7 V and a constant current density of 1 $A{\cdot}g^{-1}$). Irrespective of the type of MXene studied as symmetric supercapacitor in aqueous electrolyte, electrochemical data are limited to a very narrow voltage window (usually < 1.0 V).

Considering the huge interest in developing MXene-based ultralight and flexible supercapacitors for electronic applications, it goes without saying that similar (if not more) research attention should be paid toward the development of the lightest MXene (Ti_2CT_x) for enhanced supercapacitance. Theoretically, Ti_2CT_x should have a higher

*Electrochemical Society Member.
[z]E-mail: Kenneth.ozoemena@wits.ac.za

gravimetric capacitance than $Ti_3C_2T_x$ as it has a higher theoretical surface area per gram (i.e. $Ti_3C_2T_x$ has one inaccessible TiC layer). Motivated by this understanding, this work is focused on tuning the synthesis of Ti_2CT_x and modifying it with carbon nanospheres (CNS) for enhanced supercapacitor performance in 1 M Li_2SO_4 aqueous electrolyte. To our surprise, a high-voltage (1.5 V) symmetric supercapacitor was achieved with satisfactory power and energy densities in this neutral aqueous electrolyte. This is the first report of a MXene-based high-voltage symmetrical supercapacitor in an aqueous electrolyte.

Experimental Procedure / Methodology

Materials and method.—The MXene Ti_2CT_x was prepared from the commercially available Ti_2AlC MAX phase powder (Maxthal 211, Kanthal AB, Sandvik Materials Technology, Sweden; >90% wt purity; <45 μm particle size) by selective exfoliation of the aluminum following a slight modication of the procedure developed by Naguib et al.[2,42] In summary, 10 g of Ti_2AlC MAX phase powder was slowly added into 100 ml of 40% Hydrofluoric (HF) acid solution (Gold line, CP, Associated Chemical Enterprises Pty Ltd) in a plastic container and stirred with a magnetic stirrer for 2.5 h at room temperature. The obtained suspension was washed several times with copious amounts of distilled deionized water; each time, the suspension was left to settle and the supernatant liquid decanted. After several washings to dilute the acid solution using this settling and decanting process, the suspension was finally subjected to more washing with distilled deionized water, separated each time by centrifugation. The process was continued until a pH of 5–6 was reached. The resultant MXene Ti_2CT_x powder (denoted herein as **MX**) was then oven-dried at 70°C for 4 days.

Carbon Nano Spheres **(CNS)** were synthesized by direct pyrolysis of hydrocarbon gas in the Chemical Vapor Deposition (CVD) method. Acetylene (C_2H_2) gas (AFROX, Instrument grade N2.0, 508103-DC-C, ≥ 99.0% purity) as the carbon source, and Argon (Ar) (AFROX, Baseline 5.0, 512203-SE-C, ≥ 99.999% purity) as carrier gas, were passed through a tubular quartz reactor (5 cm inner diameter and 100 cm length), which was placed vertically in a furnace. The heating rate and reaction temperature in the furnace were electronically controlled. The gases flow rates were controlled using Cole-Parmer n082-03 rotameters (reading of the scale was translated to flow rate of the relevant gas).[43] Prior to the synthesis and during heating to the required reaction temperature of 1000°C, the quartz tube was flushed with Ar, to remove all air, at a flow rate of 330 ml·min^{-1}. When the reaction temperature was reached, C_2H_2 at a constant flow rate of 290 ml·min^{-1} was added to the Ar carrier gas. The product was deposited on the inner wall of the quartz tube and carried by the gas flow to the product collection chamber. The reaction was held at these conditions for 30 min, after which the flow of C_2H_2 was stopped and the system was allowed to cool to room temperature (about 6 hours) under Ar gas flow. After cooling, the product was collected from both the quartz tube and the collection chamber.

Material characterization.—Powder X-ray diffraction (PXRD), to confirm material phase identities, was performed on as-synthesized powder samples, using Bruker D2 Phaser Desktop Diffractometer (Bruker AXS, Karlsruhe, Germany) with Lynxeye detector using Co Kα radiation of wavelength 1.78897 Å. The diffraction angles ranged between $2\theta = 7^\circ$ to $2\theta = 100^\circ$, with a step size of 0.0260°. The generator settings were 30 kV and 10 mA. The Bruker DIFFRAC.SUITE EVA software with ICDD PDF-4+ database was used to identify the phases from the patterns. The X-ray photoelectron spectroscopy (XPS) measurements were performed using an AXIS ultra DLD spectrometer (Kratos Analytica) equipped with a monochromatic AlKa excitation source (1486.6 eV) to investigate the oxidation states of the elements in the samples. The deconvolution of the obtained XPS high resolution core-levels was carried out using CasaXPS Version 2.3.16. Scanning electron microscopy (SEM) images, for morphology characterization, were collected using an FEI Nova Nanolab 600 FIB/SEM instrument operating at 30 kV. The samples were loaded on a carbon tape and were coated with a gold-palladium alloy layer to avoid electric charging of the samples. Transmission electron microscopy (TEM) images, for morphology characterization, were collected using an FEI Tecnai T12 Spirit electron microscope (FEI Co., Hillsboro, OR, USA), operated at an accelerating voltage of 120 kV. The samples were ultra-sonicated in ethanol and loaded onto a carbon-coated copper grid. Elemental composition was obtained using Oxford INCA energy dispersive X-ray spectroscopy (EDS) systems on the TEM and SEM. Raman spectra, to help determine the structural composition of the materials, was collected using a Horiba LabRAM HR micro-Raman spectrometer equipped with an Ar ion laser (514.5 nm, 0.5 mW at the sample) as the excitation source. Backscattered spectra were collected using an Olympus BX41 microscope attachment (100x objective), and the light was dispersed with 600 lines per millimeter gratings onto a liquid nitrogen–cooled CCD detector. Spectra were processed using LabSpec v5 software. Specific surface area (SSA) and porosity were measured using Micromeritics TriStar II 3000 area and porosity analyzer instrument. Prior to testing, a sample of about 0.2 g was degassed in N_2 at 150°C for 4 hours or 90°C overnight and the surface area measurements were performed via N_2 adsorption/desorption at −196°C and calculated by the Brunauer Emmett and Teller (BET) analysis method in the relative pressure range P/P0 = 0.05–0.35. Total pore volumes of the samples were calculated at a relative pressure of P/P0 = 0.99.

Fabrication and evaluation of MX/CNS-based electrodes and cells.—Electrochemical performance was investigated for conventional three-electrode system (half-cell) and two-electrode symmetric system (full or single cell) configurations. The active electrode material was obtained by thoroughly mixing MX, CNS, carbon black (CB) (PRINTEX XE-2-B, Degusa) as a conducting agent and Polyvinylidene fluoride powder (PVDF) (Sigma-Aldrich) as a binder in a weight ratio of 76:4:15:5, respectively, using mortar and pestle. A few ml of *N*-Methyl-2-pyrrolidone (C_5H_9NO) (NMP) (ReagentPlus, 99%, Sigma-Aldrich) was added as a wetting agent, to produce homogeneous slurry. For the three-electrode configuration, the slurry was coated on to a Ni foam which acted as a current collector (Celmet: thickness = 1.6 mm) using a spatula at a mass loading range of 1–2 mg·cm^{-2}, and dried at 90°C in a vacuum oven for 15 h. The Ni foam was cleaned, prior to use, by sonicating for 30 min in a 1 M HCl solution and washing with copious amount of distilled de-ionized water. The process was repeated twice, after which the Ni foam was dried overnight in a vacuum oven. An over-sized platinum net was used as the counter electrode, Ag|AgCl (3 M KCl) as the reference electrode, and 1 M Li_2SO_4 (ACS reagent, ≥ 99.0% wt, Sigma-Aldrich) aqueous solution as the electrolyte. The cell was allowed to equilibrate for 2 h prior to electrochemical testing. For the two-electrode symmetric cells, slurries were pasted on Al foil current collector and dried at 90°C in a vacuum oven for 18 h, after which electrodes with a diameter of 15 mm were cut out. Two symmetric MX/CNS electrodes, separated by a glass microfiber filter (Whatman GF/F) in a 1 M Li_2SO_4 aqueous solution were sandwiched in a supercapacitor coin-type cells (CR 2032) or Swagelok cells (MTI, Inc., USA). Stainless steel spacer and spring were inserted between the case and the negative electrode for better fitting. After assembly, the coin cells were pressed at 500 psi and left for complete soaking of all components in the electrolyte for 18 h, prior to testing. Electrochemical measurements on both three-electrode and two-electrode symmetric cells were performed at room temperature and using cyclic voltammetry (CV), galvanostatic cycling with potential limitation (GCPL), and electrochemical impedance spectroscopy (EIS). The testing was performed using computer controlled multichannel potentiostat/galvanostat Bio-Logic VMP3, driven by EC-Lab v10.40 software. The CV tests were conducted at scan rates varying from 5 to 1000 mV·s^{-1}. The GCPL tests were carried out at varying current densities from 0.1 to 10 A·g^{-1}. EIS measurements were carried out in the frequency ranging from 200 kHz to 10 mHz at an open circuit voltage with AC voltage amplitude of 3 mV and Z-fit tool was used for data analysis. Constant voltage-holding (floating)

experiments were performed by holding for 10 h at a specific voltage, then three charge-discharge cycles were carried out. This process was repeated five times for a total of 50 h.

The properties of the EC cells and electrodes, i.e., specific capacitance, energy density, power density and maximum power density are calculated from the discharge part of the GCPL curves. The capacitance, C (F) is given by the well-established Equations 2, 3 and 4 when calculated from GCPL, EIS or CV results, respectively.[44,45]

$$C = \frac{I\Delta t}{\Delta V} \quad [2]$$

$$C = -\frac{1}{2\pi f z''} \quad [3]$$

$$C = \frac{(\int I(t)\,dt)/2}{V} = \frac{(\int I(V)\,dV)/2}{\upsilon \cdot V} \quad [4]$$

where I (A) is the applied current, ΔV (V) is the discharge voltage window excluding the IR drop, Δt (s) is the corresponding discharge time, f (Hz) is the frequency, z'' (Ω) is the imaginary part of the impedance, $\int I(V)dV$ is the integration of the area enclosed by the CV, when near rectangular, divided by 2 to account for the discharge part, υ (mV·s^{-1}) is the scan rate and V (V) is the voltage window for the CV curve. Specific capacitance, C_{sp} (F·g^{-1}, F·cm^{-3} and F·cm^{-2} for gravimetric, volumetric and geometric specific capacitances, respectively) for the three-electrode systems or half-cells is calculated by Equation 5.

$$C_{sp} = \frac{C}{S} \quad [5]$$

where S is the mass (g) or the volume (cm^3) or the geometric area (cm^2) of the active material. In the case of a symmetric cell, where both the working and counter electrodes are of the same material, size, mass and thickness, the specific capacitance, C_{sp} per electrode (F·g^{-1}, F·cm^{-3} and F·cm^{-2} for gravimetric, volumetric and geometric specific capacitances, respectively) is evaluated by Equation 6.

$$C_{sp} = \frac{4\,C}{S} \quad [6]$$

where S is the mass (g) or the volume (cm^3) or the geometric area (cm^2) of the active material of both electrodes. The energy density, power density and maximum power density are calculated from GCPL results. Gravimetric energy density, E_{sp} (W·h·kg^{-1}), is calculated using Equation 7.[44]

$$E_{sp} = \frac{C\Delta V_{max}{}^2}{2m} \cdot \frac{1000}{3600} \quad [7]$$

where ΔV_{max} (V) is the maximum voltage region applied and m (kg) is the mass of the active material in both electrodes. The gravimetric power density, P_{sp} (W·kg^{-1}) is calculated according to Equation 8.

$$P_{sp} = \frac{E_{sp} \cdot 3600}{\Delta t} \quad [8]$$

The maximum power density, P_{max} (W·kg^{-1}) is evaluated by Equation 9.[44]

$$P_{max} = \frac{\Delta V_{max}{}^2 \cdot 1000}{4m \cdot ESR} \quad [9]$$

where ESR (Ω) is the equivalent series resistance of the system, determined from the initial voltage drop between the first two points at the beginning of the discharge curve. In the case where discharge comes immediately after charge by switching the current, it is determined by Equation 10.[46]

$$ESR = \frac{\Delta V_{iRdrop}}{2I} \quad [10]$$

where ΔV_{iRdrop} (V) is the voltage drop between the first two points after the switch to discharge.

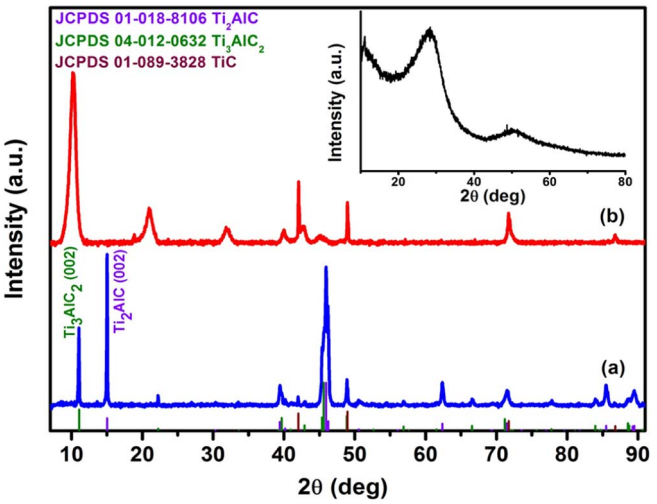

Figure 1. XRD patterns of Ti_2AlC powder (Maxthal 211) before treatment with HF (a) and after etching with 40% HF for 2.5 h (b). Inset: XRD patterns of CNS.

The coulombic efficiency η (%) is calculated by Equation 11.

$$\eta = \frac{t_d}{t_c} \cdot 100\% \quad [11]$$

where t_d and t_c are the discharge and charge times, respectively.

Results and Discussion

Material characterization.—Figure 1 shows the PXRD patterns of the Maxthal 211 powder before and after exfoliation. The as-received Maxthal 211 powder before etching (Figure 1a) consists mainly of Ti_2AlC (JCPDS 01-081-8106), with minor quantities of Ti_3AlC_2 (JCPDS 04-012-0632), TiC (JCPDS 01-089-3828) and Ti_xAl_y (JCPDS 04-007-2382, 01-074-4925, 04-007-2383 and 01-081-9785). These phases were also observed by other researchers who worked with the same material obtained from the same source.[47–51] After treatment with HF (Figure 1b), the intensity of the main peaks of Ti_2AlC and Ti_3AlC_2 decreases. The (002) peak broadens and a shift to lower angles - higher d-spacing, is observed. This correlates with the formation of MXene, i.e. replacement of Al with = O, OH or F.[2,36,42,52–56] TiC (JCPDS 01-089-3828) and TiO_2 (JCPDS 00-021-1272) can also be identified in the samples as also observed by others.[24,32] The other unknown peaks may be related to some MXene surface oxides arising from prolonged drying of MXene in air. However, further studies are needed to understand the origin of these peaks.

The PXRD pattern of CNS can be seen in the inset of Figure 1. Two wide diffraction peaks can be clearly identified, centered at ~29° and ~51°. These peaks can be indexed to the (002) and (100) graphite planes (JCPDS 00-041-1487). The relatively low and broad shape of the (002) peak implies that the CNS is composed of turbostratic carbon with weakly ordered graphene layers that are randomly rotated with respect to each other.[57,58]

Figure 2 displays the Raman spectra of the Maxthal 211 powder before and after exfoliation. The peaks ω_1, ω_2 & ω_3 and ω_4 in spectrum (a) are at 149.3, 267.8 and 360 cm^{-1}, respectively. These peaks, are the main characteristic peaks of Ti_2AlC and are in good agreement with literature[36,59–62] where they are assigned to the shear and longitudinal vibrations of the Ti and the Al atoms.[63] Specifically, ω_1 is associated with vibrations of the Al, and its disappearance in spectrum (b) correlates with the removal of the Al and the formation of MXene. The peaks in spectrum (b) are upshifted and broadened as compared to the peaks in spectrum (a). The upshift can be attributed to intercalation of surface groups due to the etching process.[64] The broadening of the peaks in spectrum (b) corresponds with decrease in

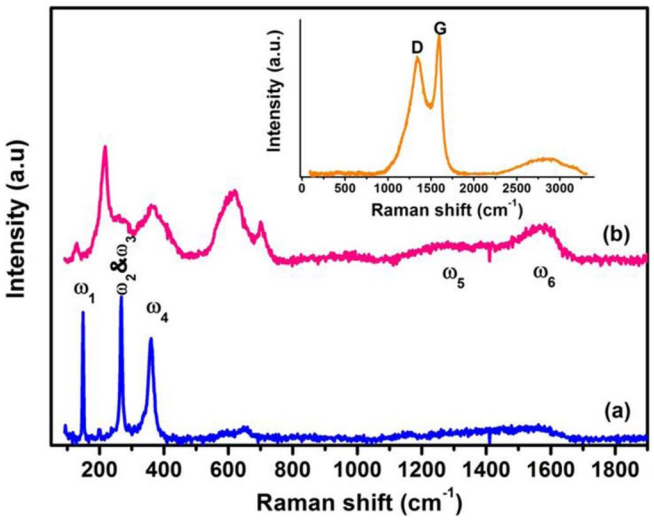

Figure 2. Raman spectra of Ti2AlC powder (Maxthal 211) before treatment with HF (a) and after etching with 40% HF for 2.5 h (b). Inset: Raman spectrum of the CNS.

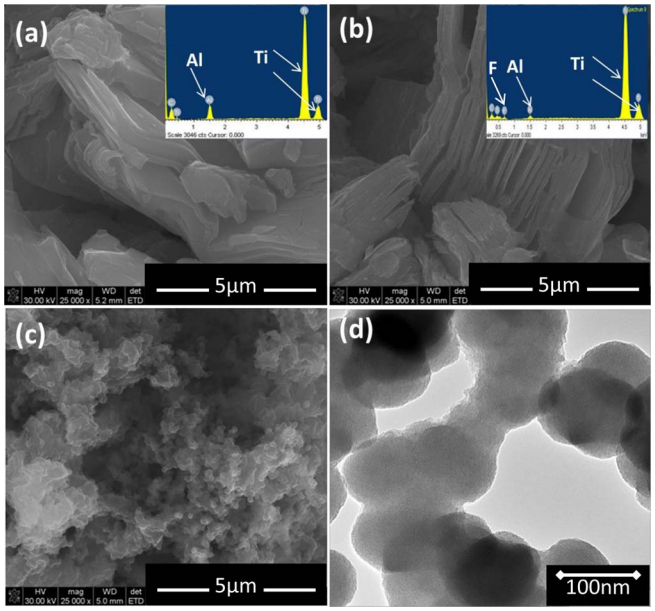

Figure 3. SEM images of Ti_2AlC powder (Maxthal 211) before treatment with HF (a) and after etching with 40% HF for 2.5 h (b). The insets are the EDS analysis of both samples. SEM image of the CNS (c) and TEM image of the CNS (d).

order as is expected by the exfoliation process and was also observed in the XRD spectrum discussed above (Figure 1b).[64] The broad peak at ~630 cm^{-1} may be attributed to non-stochiometric TiC_x.[6,65] The broad weaker bands ω_5 and ω_6 at around 1350 cm^{-1} and 1580 cm^{-1}, respectively, are likely the characteristic D- and G-bands of carbon, associated with the presence of some free carbon and disorder in the samples. Both G and D peaks are due to sp^2 sites. The G-band peak is associated with the stretching of the C-C bond in carbon materials and is common to all sp^2 carbon systems both rings and chains. The D peak depends on sp^2 fraction and order and appears only if the sp^2 is in disordered rings.[66,67]

Figure 2 inset displays the Raman spectra of the synthesized CNS. As expected, the obtained peaks are the D and G bands at 1337.2, and 1595.4 cm^{-1}, respectively, as discussed above. The relative intensities of the D and G peaks (I_D/I_G) are commonly used to evaluate the graphitic character. The value of (I_D/I_G) obtained here is 0.84 and was measured by dividing the relevant intensities of the peaks. This value is within the range of obtained ratios in literature denoting that the degree of graphitization is not high.[58,68] These results corroborate the observations from the XRD results above.

The SEM and TEM images of the Ti_2AlC powder (Maxthal 211) before and after treatment with HF as well as of the CNS are presented in Figure 3. The gaps left by the successful etching of the Al layer can be clearly seen in the SEM picture in Figure 3b as compared to Figure 3a, as well as the sharp decrease in Al and appearance of F that can be seen in the relevant EDS elemental analysis in the insets, which clearly shows that the intensity of the Ti in the precursor MAX phase is the same as in the final MXene. This is also supported by the rise in magnitude in the calculated BET specific surface area (SSA) from 1.7 $m^2 \cdot g^{-1}$ in the MAX phase to 20.2 $m^2 \cdot g^{-1}$ in the MXene, which are in agreement with literature[6,11,24,35,36] These findings strongly support the results obtained above in XRD and Raman indicating the raise in disorder of the obtained materials. In Figure 3d the randomly oriented graphene planes comprising the CNS are evident, supporting the conclusions from the XRD and Raman data.

Electrochemical characterization.—Figure 4a shows the CV behavior of the individual CNS, MX and combined MX/CNS electrodes in a three-electrode system in 1 M Li_2SO_4 electrolyte at 20 mV·s^{-1}. These results show that the combination of MX and CNS has an improved capacitance as compared to the individual components MX and CNS.

It is clearly observed that the capacitance of CNS alone is extremely low. It can also be seen that at lower voltage change rates the additional effect of the added CNS is more significant. Figures 4b and 4c display the CV curves at different scan rates and GCPL curves at different gravimetric current densities of the combined MX/CNS composite materials. The CV curves in Figure 4b have a shape that is proximate to rectangular, which corresponds to good reversible capacitive behavior, but still differ from the ideal rectangular shape for the EDLC. This is also demonstrated by the nearly isosceles triangle shape of the CD curves in Figure 4c, indicating good coulombic efficiency calculated as between 92–97%. These results suggest that pseudocapacitive Li^+ intercalation reactions occur at the electrodes as described in Equation 1. Above 100 mV·s^{-1}, the CV curves in Figure 4b become less rectangular indicating a more resistive character. This distortion may be because of greater difficulty for Li^+ ions to diffuse into or out of the materials' structure as the rate increases, therefore limiting effective interaction of the cations with the electrode surface to shallower adsorption sites.[19,69–71] This behavior can also explain the line becoming rounded during charging at the higher voltages for the lower current density of 1 A·g^{-1}. Both the CV scans and the GCPL curves show no peaks. The absence of peaks suggests that the same pseudocapacitive behavior, probably lithiation and delithiation as in Equation 1, occurs over the entire cycle.

Figure 4d presents the comparative results of specific gravimetric capacitance of the individual components MX and CNS, and their combination MX/CNS, at different gravimetric current densities. As can be seen from these results, the capacitance of the MX material, and MX combined with CNS, decreases with the increase of the gravimetric current density. It can also be observed here, as was seen in Figure 4a, that the capacitance of CNS is extremely low as compared to the MX. However, the combination of MX with the CNS yields improved capacitance by more than 15%. The same finding was observed for the GCPL experiments (data not shown). This is quite significant if one considers that CNS constitutes a mere ca. 4% of the active electrode materials. Such improvement may be ascribed to (i) increased content of the high-surface area CNS on the surface of the MXene (as discussed later, XPS data show that MXene is mainly carbon) and / or (ii) the ability of the CNS to assist in expanding the interlayer spacing of the MXene for improved ion transport (exemplified in Figure 5). Although the MX/CNS electrode was obtained by a simple mixing of MX and CNS, Figure 5 clearly shows that the possibility of some of the CNS (~100 nm) and other additives used in this work getting

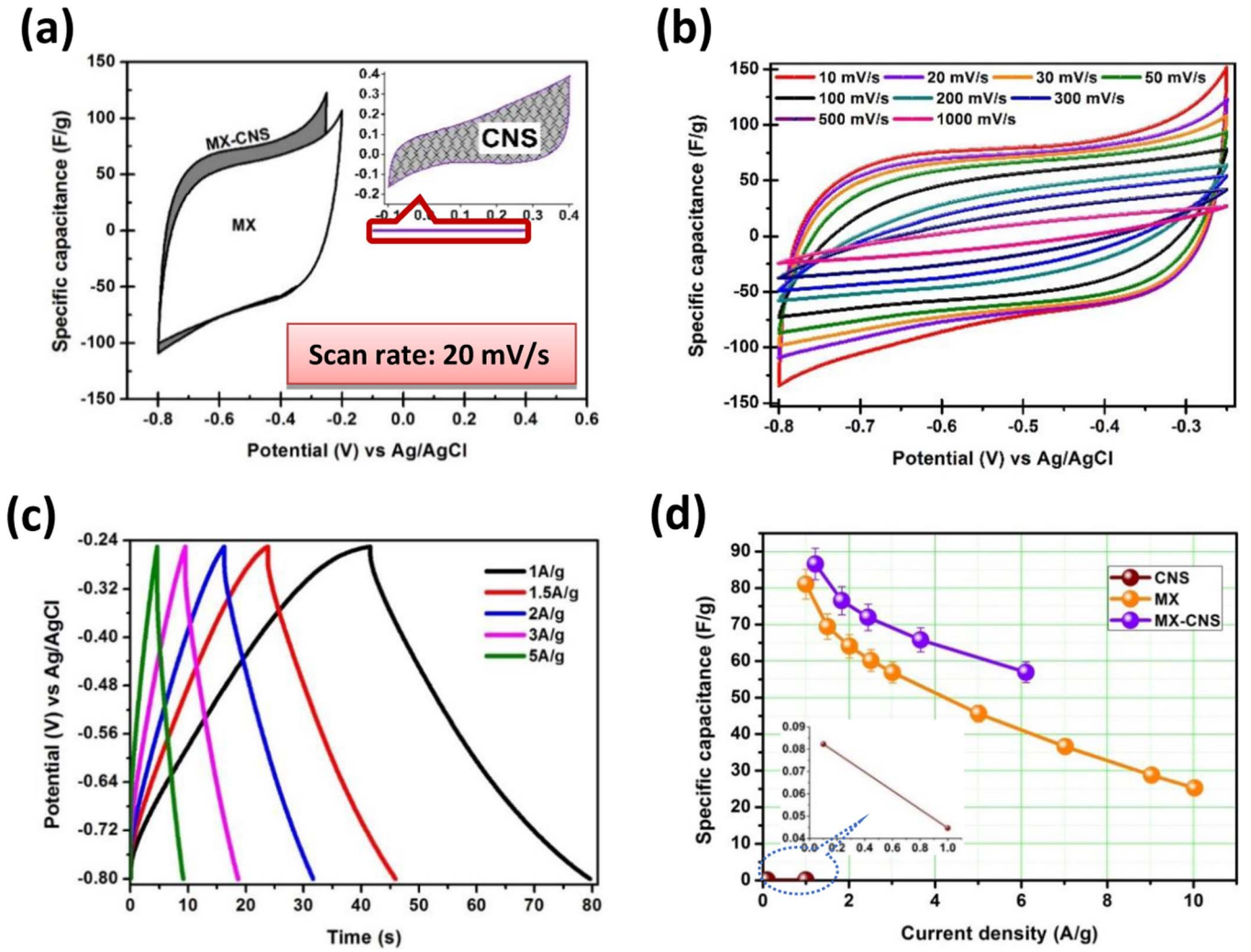

Figure 4. Cyclic Voltammetry (CV) compared curves of MX, CNS and MX/CNS at (a) 20 mV· s^{-1}; (b) CV curves of MX/CNS at various scan rates; (c) GCPL curves of MX/CNS at various gravimetric current densities and (d) GCPL compared results of specific capacitance at varying gravimetric current densities of MX, CNS and MX/CNS. All data acquired in a three-electrode system with 1 M Li_2SO_4 electrolyte. In CV curves (a, b), the measured current is normalized by the scan rate and working electrode active material mass, resulting in the virtual F·g^{-1} unit.

between the large MX sheets (micron-sized) cannot be completely ruled out.

The symmetric MX/CNS electrodes were tested at increasing voltage ranges from 0.6 up to 1.8 V as can be seen in Figure 6a. Up to a voltage range of 1.5 V the curves sustain a semi-rectangular shape, pertaining to good capacitive behavior. Above 1.5 V, oxidation of the electrolyte starts to occur thus, 1.5 V is the optimal supercapacitor voltage for this device. The wide voltage range obtained stems from the use of the Li_2SO_4 electrolyte in a cell with a contained amount of water. It has been reported that symmetric supercapacitors with wide voltage range, higher than the theoretical limit of water, can be overcome with pH-neutral electrolytic solutions of inorganic salts such as Li_2SO_4, Na_2SO_4 and K_2SO_4 with the Li_2SO_4 being the most promising salt to date.[72] As explained by Fic et al.,[72] the Li^+ and SO_4^{2-} ions are strongly solvated in the water molecules. The energy needed to decompose the water competes with the solvating energy. Since the amount of water molecules is limited, it can be assumed that they are all bonded to the ions, resulting in water decomposition being delayed to 1.6 – 2.2 V instead of the expected 1.23 V theoretical limit for water. In addition to that, Srimuk et al.[73] demonstrated that the distribution of voltage in the symmetric MXene cell between anode and cathode is not symmetric as in the case of an EDLC based symmetric cell (e.g. activated carbon). In such a case, the MXene electrodes may behave as in an asymmetric cell, enabling the wider range of cell voltage, as observed in our results. To the best of our knowledge, it is the first time that such a wide voltage has been reported in a symmetric aqueous system with MXene-based electrode materials. At this juncture, it should be mentioned that many other researchers[29,37,69] have studied

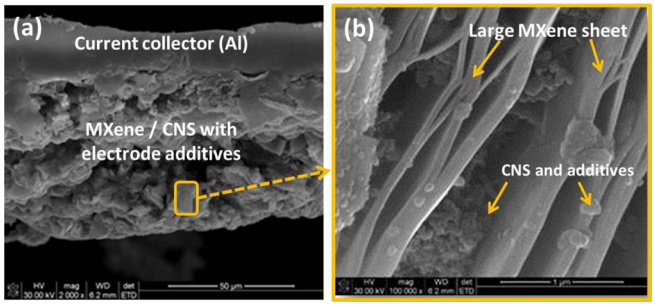

Figure 5. (a) Typical SEM image of MX/CNS composite electrode fabricated on an aluminum current collector using the same method described in the Experimental section, (b) is the expanded portion of the SEM image showing the long sheets of MXene where CNS and other electrode additives such as the carbon black are deposited on the surface or buried in the interlayer spacing of the MXene sheets.

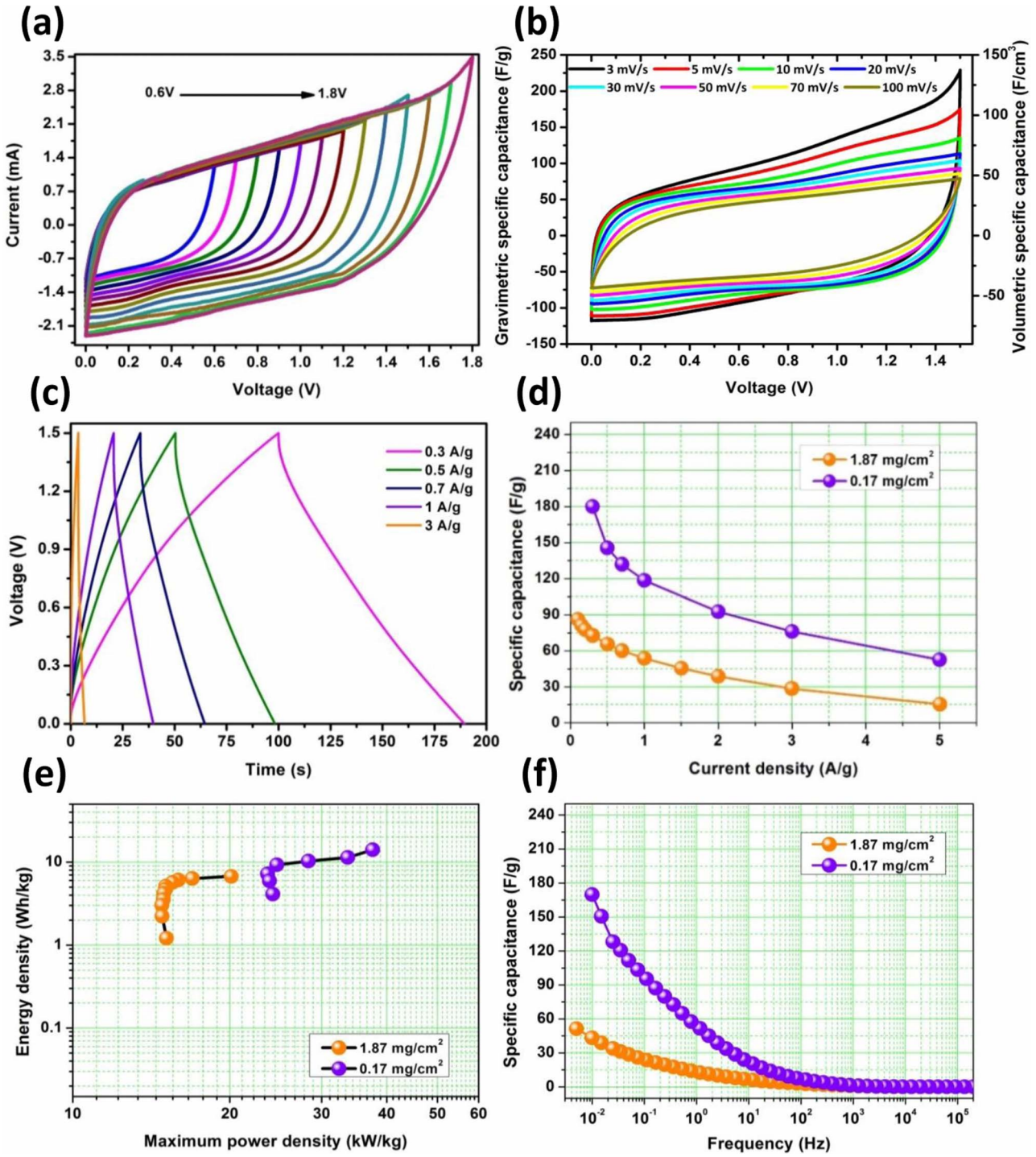

Figure 6. CV curves (a) at different voltage ranges at 20 $mV \cdot s^{-1}$ and (b) at various scan rates; (c) GCPL curves at various gravimetric current densities; (d) Specific gravimetric capacitance from GCPL at various gravimetric current densities for different electrode material mass loading; (e) Gravimetric energy density vs maximal power density for different electrode material mass loading; (f) Specific gravimetric capacitance from EIS data at various frequencies for different electrode mass loading. All data acquired for MX/CNS symmetric coin cells with 1 M Li_2SO_4 electrolyte. Data for (b) and (c) attained with an electrode mass loading of 1.87 $mg \cdot cm^{-2}$. In (b), the measured current is normalized by the scan rate and the active material mass or volume of both electrodes and multiplied by 4, resulting in the virtual $F \cdot g^{-1}$ or $F \cdot cm^{-3}$ unit.

the performance of Ti_3C_2 in the same electrolyte (Li_2SO_4) used in this work.

Figure 6b shows the CV obtained for the MX/CNS symmetric cell at various scan rates. At 20 $mV \cdot s^{-1}$ the curve has an almost rectangular shape. As the rate becomes higher, the shape becomes less rectangular, possibly because of diffusion limitations of Li^+ into the MXene structure. At lower scan rates, oxidation is evident at the higher voltages. No other peaks are evident, indicating again that the only processes occurring are the highly reversible lithiation and delithiation suggested in Equation 1. This is also reinforced by the nearly linear charge-discharge profiles in Figure 6c. These CD curves show minor IR drop and coulombic efficiency of 67.7% at 0.1$A \cdot g^{-1}$,

above 82% for 0.15–0.3 $A \cdot g^{-1}$ and between 95 and 98.5% for 0.5 $A \cdot g^{-1}$ and higher.

Figure 6d shows the specific gravimetric capacitance for two symmetric MX/CNS cells with different electrode material mass loading obtained at different current densities. The capacitance decreases with the increase of gravimetric current density with a capacitance loss of 82% between 0.1 $A \cdot g^{-1}$ and 5$A \cdot g^{-1}$. It can be seen from this figure that smaller mass loading yields a higher specific capacity of 180 $F \cdot g^{-1}$ at 0.3 $A \cdot g^{-1}$, while 86 $F \cdot g^{-1}$ at 0.1 $A \cdot g^{-1}$ is obtained for the higher mass loading. CV data also follow a similar trend (data not shown). The phenomenon of dependence of the specific capacitance on the mass loading or electrode thickness was demonstrated by others[19,20,74,75] who also attained a similar trend. This can be explained by the fact that when the mass is higher, the thickness is higher, and the penetration of the Li^+ ions to the deeper electrode layers and intercalation, which directly involves the surface of the material, is more difficult. As a result, resistance increases. In addition, part of the electrode mass is ineffective and does not contribute to the overall capacitance, therefore, leading to a lower specific capacitance.

Figure 6e shows energy density vs maximum power density of the two symmetric MX/CNS cells with different electrode material mass loading obtained at different current densities. The maximal power and energy achieved are 37.6 $kW \cdot kg^{-1}$ and 14.1 $W \cdot h \cdot kg^{-1}$, respectively, at 0.3 $A \cdot g^{-1}$ for the lower mass loading electrodes and 20.1 $kW \cdot kg^{-1}$ and 6.7 $W \cdot h \cdot kg^{-1}$, respectively, at 0.1 $A \cdot g^{-1}$ for the higher mass loading electrodes. These values are in the range or even higher than usually seen for symmetric aqueous EC.[25,76–79]

Figure 6f shows a typical plot of the specific capacitance as a function of frequency, obtained from electrochemical impedance spectroscopy (EIS) at different mass loadings. As expected, the specific capacitance increases with decrease in frequency response. At high frequencies, the cells behave as absolute resistors. Interestingly, however, the result is in excellent agreement with charge-discharge data (Figure 6b).

Considering that several researchers have shown that carbon-based symmetric supercapacitors can be operated in neutral aqueous electrolyte in high voltage, we decided to conduct XPS experiments to provide some insights into the electronic structures and carbon contents of the MXene used in this work. The results (Figure 7) demonstrate the co-existence of the main expected functional groups, namely, oxide (-O-), hydroxyl (-OH) and fluoride (-F).[80] The survey scan spectra (Figure 7a) show the expected core levels, namely, F 1s, O 1s, C 1s, Ti 2p for MXene, and O 1s, C 1s, Si 2p for CNS. Analysis of the spectra reveals the atomic percentage for each element. The obtained values for the MX sample are O 1s (32.9 at.%), C 1s (48 at.%), Ti 2p (2.6 at.%) and F 1s (16.5 at.%), clearly showing that the MXene used in this work is mostly carbon. For the CNS the atomic percentages are C 1s (88.8 at.%), O 1s (8.4 at.%) and Si 2p (2.8 at.%). GAUSSIAN deconvolution with $\chi^2 \leq 1$ was used to fit the components in the high resolution XPS core-level spectra for the MX sample (Figures 7b–7e) and the CNS sample (Figures 7f–7h), giving a more detailed picture of the materials surface structure. The obtained values of the binding energy (BE) after deconvolution are comparable with previous studies.[80–82] For the MXene, the O 1s core level consists of three photoelectron peaks (Figure 7b). The lower BE, located at 529.38 eV, which comprises 57.59% of the photoemission in the O 1s core level is assigned to TiO_2 formed by oxidation of the MXene surface.[81–83] The medium BE, located at 530.84 eV is assigned to C-Ti-O_x and comprises 7.73% of the O 1s photoemission.[83] The higher BE detected at 531.9 eV which account for 34.67% of the photoemission is related to C-Ti-$(OH)_x$.[11,81,83] These last two BEs can be assigned to -O_x/$(OH)_x$ terminations on the MXene surface.[2] The C 1s core level was also successfully fitted using four Gaussian components (Figure 7c) located at 280.47 (12.38% of C 1s photoemission), 283.58 (74.25%), 285.44 (6.58%) and 287.5 eV (6.78%) corresponding to C-Ti, C-C, C-N, O-C = O bonds, respectively. The large amount of C-C and the O = C-O peaks may arise from hydrocarbons formed during the etching[80] remaining after washing or formed during oxidation.[6,24] The Ti 2p core level (Figure 7d) was fitted with five components which consist of two doublets ($2p_{3/2}$ and $2p_{1/2}$). The deconvoluted peaks at BE 453.76 (9.6% of Ti 2p photoemission), 454.91 (20.22%), 458.27 (12.98%), 459.23 (42.03%) and 464.11 eV (15.8%) can be assigned to Ti-C, Ti^{2+}, Ti^{3+}, Ti-O and C-Ti-F_x, respectively.[80,84,85] The Ti-C signal may be ascribed to Ti atoms coming from the interior and can also come from TiC[83] which was evidenced from the XRD results to be present as impurity in the original MAX phase material. Ti signals with oxidation states 2+ and 3+ indicate the formation of different mixed oxides and carboxides on the MXene surface. The Ti-O signal, which is very large, may be due to oxidation of the MXene at the edges forming TiO terminations and TiO_2 aggregates.[2,11] This may come as a result of the material being exposed to air during drying. For F 1s core level (Figure 7e), two components were obtained after Gaussian fitting and can be respectively assigned to C-Ti-F_x (683.87 eV which is 64.16% of F 1s photoemission) and AlF_x (684.44 eV which is 35.84%). C-Ti-F signals observed both from the Ti 2p and F 1s can arise from the F termination on the MXene surface due to HF etching. A considerable amount of AlF_x is also detected, probably stemming from the etching residues which were not washed away.[86] The results are in good agreement with the literature.[80–85] Indeed, the XPS results show the existence of the expected functional groups and oxidation of the surface and also prove that MXene is made up of mostly carbon. If we consider that the electrode was constructed with extra carbons (4% CNS and 15% carbon black), it can easily be inferred that the high-voltage operation of this supercapacitor may be partly related to the high carbon content. It should be noted that several works show that carbon-based symmetric supercapacitors in aqueous electrolyte (e.g., Li_2SO_4) can be operated at high voltages. For example, Beguin group[87] reported that seaweed-derived carbons can be operated at 1.6 V in neutral aqueous electrolyte. So, it should perhaps not be completely surprising that our MXene materials gave a high voltage of 1.5 V.

Weingarth et al.[88] demonstrated that constant voltage-holding (floating) tests are more demanding than cycling tests and therefore are a more suitable method for determining long-term stability of ECs in a shorter time span. A floating test was performed on an MX/CNS symmetric cell with electrode material mass loading of 0.18 $mg \cdot cm^{-2}$. The results of the obtained specific capacitance and efficiency of the cell as a function of time are shown in Figure 8a. The specific capacity after the first 10 hours decreases vastly to about 33% of the initial capacity, probably related to the degradation due to the use high voltage operation and/or oxidation of the MXene, but thereafter remains constant for 40 hours, with an effective efficiency higher than 110%, which means that the charge time is shorter than the discharge time. As with the voltage-holding experiment, long-term repetitive galvanostatic charge-discharge cycling showed similar deterioration with time (not shown here). The unstable cycling data may be related to the use of the high voltage and/or oxidation of the MXene as was also observed by Levi at al.[69] who noted that in long-time CV cycling, at potential sweeps beyond 1.1 V, there is deterioration due to changes in the mechanical properties of the electrodes related to electrode oxidation and associated with hydrodynamic dissipation phenomena occurring at the solid-liquid interface.

EIS is employed to better understand the characteristics of the electrode-electrolyte interface and the charge transfer between them. For that purpose, the impedance data obtained over a range of frequencies is fitted with an electrical equivalent circuit (EEC). Figure 8b compares the Nyquist plots prior to and after the 50-hour voltage-holding experiments, fitted with the EEC shown in Figure 8b inset. This EEC comprises of the elements R_s, R_{ct1}, R_{ct2}, Q_1 and Q_2 described here. R_s represents the solution's ohmic resistance of the electrode system due to electric resistivity of the electrolyte, separator and electrodes. It is also known as the Equivalent Series Resistance (ESR). At the high frequency region, the diameter of the semicircle represents the charge transfer resistance (R_{ct1}) due to the electrolyte-accessible electrode surface area as well as the electrical conductivity of the electrode material (i.e., R_{ct1} decreases as the electroactive surface and conductivity of the electrode increase). The R_{ct2} describes the charge-transfer resistance due to possible faradaic (redox) activities occurring

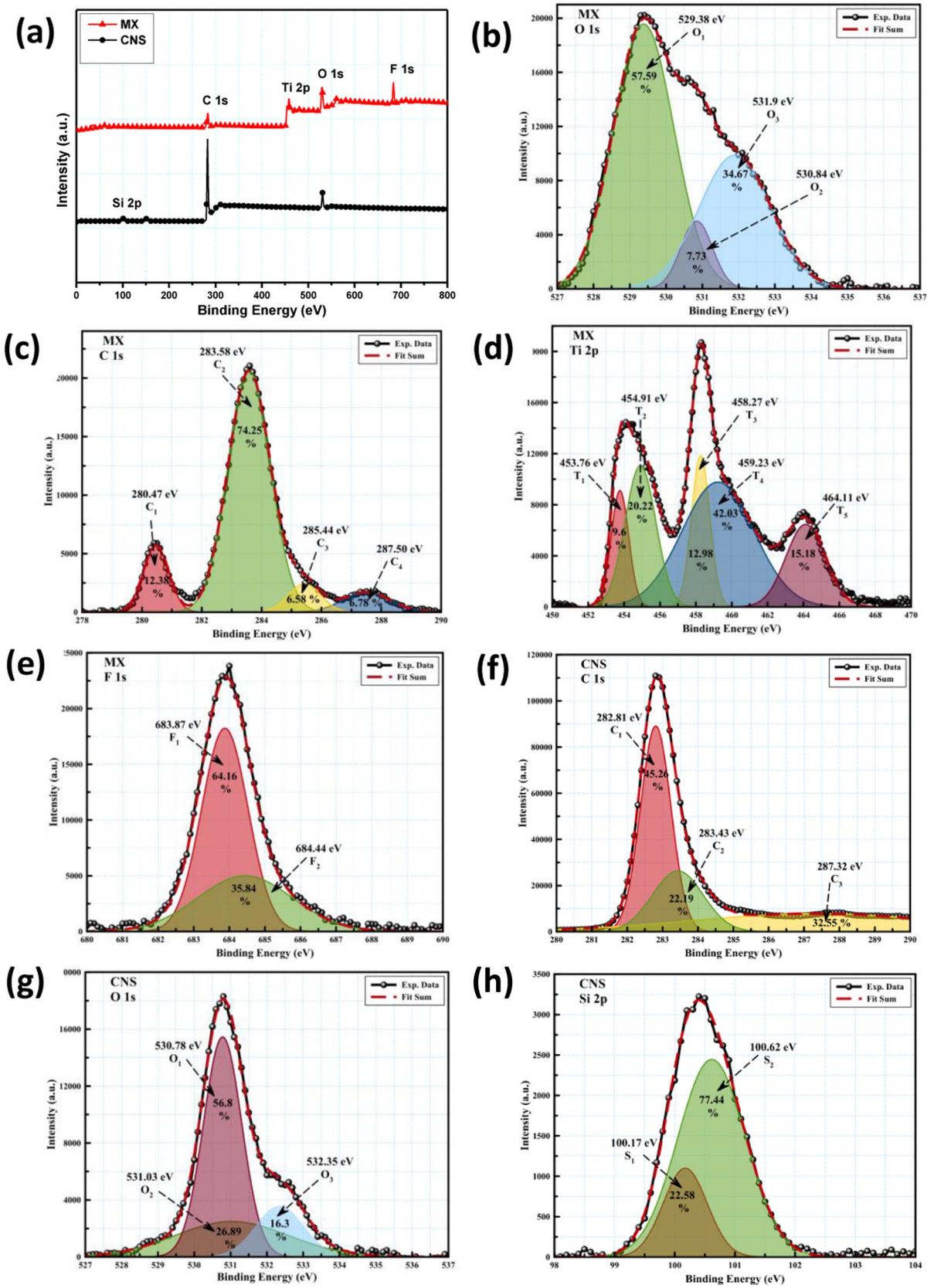

Figure 7. (a) XPS survey spectra of MX and CNS samples. (b),(c),(d) and (e) are the MX deconvoluted high resolution O 1s, C 1s, Ti 2p and F 1s core levels, respectively. (f),(g) and (h) are the CNS deconvoluted high resolution C 1s, O 1s and Si 2p core level spectra, respectively.

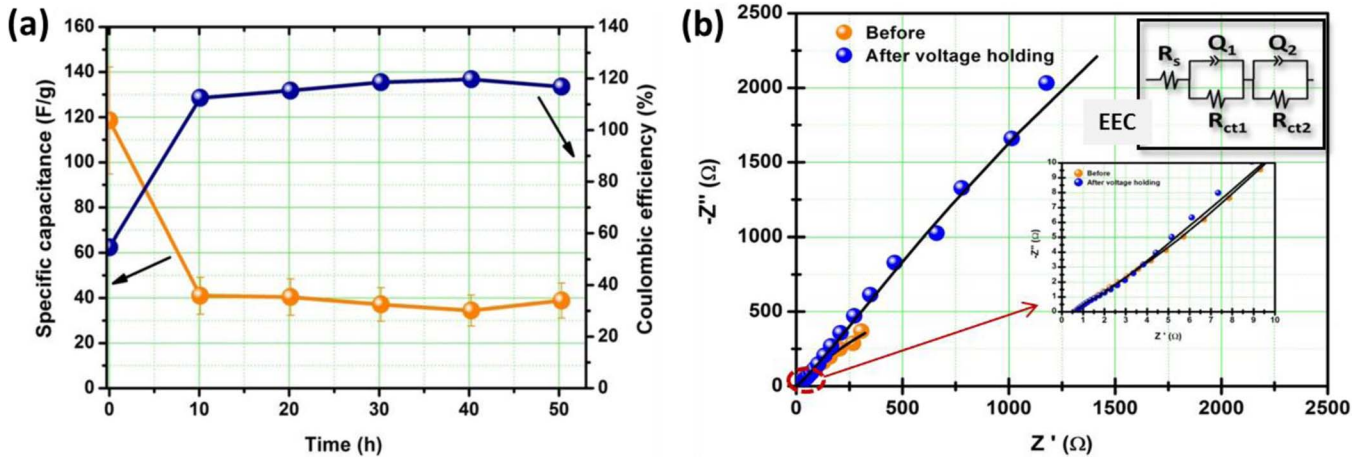

Figure 8. Electrochemical test data for MX/CNS symmetric cells with electrode material mass loading of 0.18 mg cm^{-2}: (a) Specific capacitance and efficiency as a function of time for 50 hours voltage holding experiment, capacitance measured at 0.7 $A{\cdot}g^{-1}$; (b) Nyquist plots before and after the 50 hours voltage-holding experiment, with the electrical equivalent circuit (EEC) used to fit the experimental EIS data. The arrow-indicated inset is the expanded portion of the high-frequency region. Data acquired in a Swagelok type cell with 1 M Li_2SO_4 electrolyte.

within the cell, which may corroborate the hypothesis that a symmetric MXene/CNS system may behave like an asymmetric cell. Q_1 and Q_2 represent the corresponding constant-phase elements (CPE) referring to the capacitance arising due to the heterogeneous nature of the MXene/CNS composites. The impedance of CPE is represented by Equation 12:

$$Z_{CPE} = \frac{1}{[Q(j2\pi f)^n]} \quad [12]$$

where $j = \sqrt{-1}$, Q is a frequency-independent constant that relates to the interface, n is derived from the slope of log Z plotted vs. log f (with values $-1 \leq n \leq 1$). When n takes a value close to 1, the CPE is equivalent to a capacitor and when n is close to 0 it resembles a resistor. For a value close to 0.5 the CPE impedance resembles Warburg impedance which represents ion diffusion, and when close to -1, it resembles an inductor. It is well known that CPE is a consequence of any one of the following or a combination of them: (i) the nature of the electrode material (such as porosity, roughness, or polycrystallinity), or (ii) the differences arising from the manner in which the relaxation times are distributed as a result of the heterogeneous nature of the electrode/electrolyte interface, or (iii) the fluctuations in the rate of diffusion of ions (i.e. dynamic disorder) at the electrode/electrolyte interface. The values of R_s (ESR), R_{ct}, Q and n obtained from the fitting of the EEC are given in Table I. The low values of the ESR and R_{ct1} indicate efficient interfacial electrode-electrolyte interfacial resistance of the MXene/CNS cell. The values of n here are greater than 0.5 confirming the pseudocapacitive behavior of the electrodes, becoming more capacitive after the 50-hour voltage-holding test. From the total series resistance ($R_s + R_{ct1} + R_{ct2}$) in Table I, the total resistance prior to voltage-holding is 265 Ω, while at the end of the 50-hour experiment it is 1306 Ω. The increase in impedance may be due to gradual deformation of the Mxene/CNS-electrolyte interface during voltage-holding experiments.

Table I. Comparative fitting parameters for the EIS data for MX/CNS symmetric Swagelok cell with electrode material mass loading of 0.18 mg cm^{-2} before and after 50 h voltage holding experiment fitted using the EEC. Fitting errors are less than 1%.

Parameter	Before holding test	After holding test
R_s / Ω	0.5776	0.5962
Q_1 / mF $s^{(n-1)}$	6.002	0.0797
n_1	0.633	0.9826
R_{ct1} / Ω	3.79	6.3042
Q_2 / mF $s^{(n-1)}$	11.89	4.4520
n_2	0.5026	0.7828
R_{ct2} / Ω	260.2	1299.3

Mathematical modelling and simulation.—The performance of the MXene/CNS symmetric ECs was modelled and simulated. The experimental parameters of the present work were entered into the simulation along with data extracted from literature. Details of the mathematical derivations and simulation details are described elsewhere.[89] Using the simulation, the *cell* specific capacitance $C_{spec\ cell}$ ($F{\cdot}g^{-1}$) was calculated using Equation 13:

$$C_{spec\ ,cell} = \frac{\int_0^{t_{dis}} i_{cell} dt}{M_{sy} \cdot V_{cell}} = \frac{i_{cell} \cdot \Delta t_{dis}}{M_{sy} \cdot V_{cell}} \quad [13]$$

where i_{cell} (A) is the cell current, V_{cell} (V) is the cell voltage, t_{dis} is the time of discharge and M_{sy} is the mass of the cell which includes the mass of the two electrodes, separator, and electrolyte in the cell.

The energy density ED_{sy} ($W{\cdot}h{\cdot}kg^{-1}$) and power density PD_{sy} ($W{\cdot}kg^{-1}$) were calculated according to Equations 14 and 15:

$$ED_{sy} = \frac{E_{Sdis}}{M_{sy}} \quad [14]$$

$$PD_{sy} = \frac{E_{Sdis}}{M_{sy} \cdot t_{dis}} \quad [15]$$

where E_{Sdis} (W·h) is given by Equation 16:

$$E_{Sdis} = \frac{C\left(U_{Sbdis}^2 - U_{Sedis}^2\right)}{2} \cdot \frac{1000}{3600} \quad [16]$$

where C is the capacitance of the cell, U_{Sbdis} is the cell voltage before the beginning of discharging process and U_{Sedis} is the cell voltage at end of discharging process.

Figure 9 shows the results of the simulation as compared to the experimental results obtained for (a) specific gravimetric capacitance for a whole cell vs current density and (b) gravimetric energy density vs gravimetric power density at different electrode material mass loadings and corresponding simulation results. It can be seen that there is an excellent correlation between the experimental results and the simulation. Similar correlations were observed for energy and power densities vs current densities (data not shown). The differences arise from the fact that in the experimental results, only the mass of the active material is taken into consideration in the calculations, while in the modelling the mass includes the mass of the electrodes, separator and electrolyte. Moreover, the porous electrode theory used for deriving

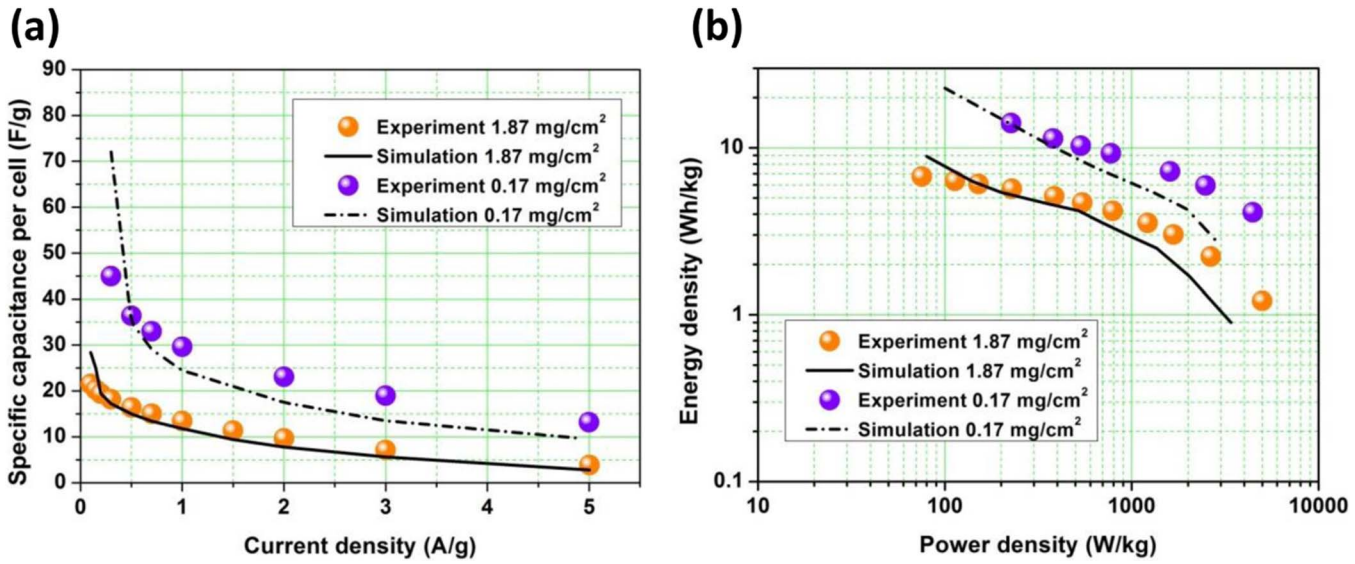

Figure 9. (a) Specific gravimetric capacitance for a cell vs current density for different electrode material mass loadings and corresponding simulation results; (b) Gravimetric energy density vs gravimetric power density for different electrode material mass loadings and corresponding simulation results. All data acquired for MX/CNS symmetric coin cells with 1 M Li_2SO_4 electrolyte.

the model equations does not account for heterogeneous microstructure of electrodes like morphology, pore size, and pore connections. Furthermore, 1-D model employed will causes a slight deviation of the experiment results from the modelling. Nevertheless, the results show good correlation.

Conclusions

The electrochemical performance of one of the lightest MXene (Ti_2CT_x) material, modified with a small amount of carbon nanospheres (CNS) to slightly open up the interlayer spacing, has been investigated. When assembled into symmetric cells and operated in aqueous electrolyte, a relatively high voltage window of 1.5 V was obtained, which is the first such observation for MXene containing electrodes in an aqueous electrolyte. The ability to undergo long-term cycling is found to be limited, suggesting the need for future improvement. Electrodes were fabricated with relative high (1.87 mg·cm^{-2}) and low (0.17 mg·cm^{-2}) mass loading and performance results were compared. Specific capacitance, maximal specific power and specific energy for the lower electrode mass loading were all higher (180 F·g^{-1}, 37.6 kW·Kg^{-1} and 14.1 W·h·Kg^{-1}) than for the higher mass loading (86 F·g^{-1}, 20.1 kW·Kg^{-1} and 6.7 W·h·Kg^{-1}). This phenomenon can be explained by the Li^+ ions' greater difficulty to penetrate the electrode materials and intercalate, in the thicker electrode, thus resulting in a higher resistance and lower electrochemical properties. Modelling and simulation of the EC correlate well with the experimental results, validating the model. The use of light-weight MXene to fabricate high-voltage symmetric supercapacitors gives promise for the realization of next-generation light-weight portable and flexible electronics. Opportunities in this area should constitute the future research direction of this work.

Acknowledgment

This study was supported by the University of the Witwatersrand (Wits). The financial assistance of the National Research Foundation (NRF), DST-NRF Centre of Excellence in Strong Materials (CoE-SM) and Wits Materials for Energy Research Group (MERG) is gratefully acknowledged. Opinions expressed and conclusions arrived at, are those of the authors and are not necessarily to be attributed to the NRF, CoE-SM and MERG.

ORCID

Sharona A. Melchior https://orcid.org/0000-0002-8901-6812
Kenneth I. Ozoemena https://orcid.org/0000-0001-7107-7003

References

1. K. I. Ozoemena and S. Chen, Eds., *Nanomaterials in advanced batteries and supercapacitors*, p. 567, Springer International Publishing, Switzerland, (2016).
2. M. Naguib et al., *Adv. Mater.*, **23**, 4248 (2011).
3. M. W. Barsoum, *MAX Phases: Properties of Machinable Ternary Carbides and Nitrides*, Wiley-VCH, Weinheim, Germany, (2013).
4. M. A. Rahman and M. Z. Rahaman, *Am. J. Mod. Phys.*, **4**, 75 (2015).
5. M. Naguib, V. N. Mochalin, M. W. Barsoum, and Y. Gogotsi, *Adv. Mater.*, **26**, 992 (2014).
6. B. Ahmed, D. H. Anjum, M. N. Hedhili, Y. Gogotsi, and H. N. Alshareef, *Nanoscale*, **8**, 7580 (2016).
7. A. Byeon et al., *ACS Appl. Mater. Interfaces*, **9**, 4296 (2017).
8. D. Er, J. Li, M. Naguib, Y. Gogotsi, and V. B. Shenoy, *ACS Appl. Mater. Interfaces*, **6**, 11173 (2014).
9. J. Halim et al., *Adv. Funct. Mater.*, **26**, 3118 (2016).
10. S. J. Kim et al., *Electrochimica Acta*, **163**, 246 (2015).
11. X. Liang, A. Garsuch, and L. F. Nazar, *Angew. Chem. Int. Ed.*, **54**, 3907 (2015).
12. Y. Liu, W. Wang, Y. Ying, Y. Wang, and X. Peng, *Dalton Trans.*, **44**, 7123 (2015).
13. C. Shen et al., *J. Electrochem. Soc.*, **164**, A2654 (2017).
14. X. Xie et al., *Nano Energy*, **26**, 513 (2016).
15. E. Yang, H. Ji, J. Kim, H. Kim, and Y. Jung, *Phys. Chem. Chem. Phys.*, **17**, 5000 (2015).
16. F. Liu et al., *J. Electrochem. Soc.*, **164**, A709 (2017).
17. M. Boota et al., *Adv. Mater.*, **28**, 1517 (2016).
18. Y. Gao et al., *J. Adv. Ceram.*, **4**, 130 (2015).
19. M. Ghidiu, M. R. Lukatskaya, M.-Q. Zhao, Y. Gogotsi, and M. W. Barsoum, *Nature*, **516**, 78 (2014).
20. S.-Y. Lin and X. Zhang, *J. Power Sources*, **294**, 354 (2015).
21. Z. Lin et al., *J. Power Sources*, **326**, 575 (2016).
22. Z. Lin et al., *Electrochem. Commun.*, **72**, 50 (2016).
23. Z. Ling et al., *Proc. Natl. Acad. Sci.*, **111**, 16676 (2014).
24. R. B. Rakhi, B. Ahmed, M. N. Hedhili, D. H. Anjum, and H. N. Alshareef, *Chem. Mater.*, **27**, 5314 (2015).
25. R. B. Rakhi, B. Ahmed, D. Anjum, and H. N. Alshareef, *ACS Appl. Mater. Interfaces*, **8**, 18806 (2016).
26. Y. Tang, J. Zhu, C. Yang, and F. Wang, *J. Alloys Compd.*, **685**, 194 (2016).
27. Y. Tang, J. Zhu, C. Yang, and F. Wang, *J. Electrochem. Soc.*, **163**, A1975 (2016).
28. Y. Tang et al., *J. Electrochem. Soc.*, **164**, A923 (2017).
29. C. Yang, W. Que, Y. Tang, Y. Tian, and X. Yin, *J. Electrochem. Soc.*, **164**, A1939 (2017).
30. C. Zhao, Q. Wang, H. Zhang, S. Passerini, and X. Qian, *ACS Appl. Mater. Interfaces*, **8**, 15661 (2016).
31. M. Zhu et al., *Adv. Energy Mater.*, **6**, 1600969 (2016).
32. J. Zhu, Y. Tang, C. Yang, F. Wang, and M. Cao, *J. Electrochem. Soc.*, **163**, A785 (2016).

33. V. Ng et al., *J. Mater. Chem. A*, **5**, 3039 (2016).
34. F. Wang et al., *J. Electrochem. Soc.*, **162**, B16 (2015).
35. M. Naguib et al., *Electrochem. Commun.*, **16**, 61 (2012).
36. F. Liu et al., *Adsorption*, **22**, 915 (2016).
37. M. R. Lukatskaya et al., *Science*, **341**, 1502 (2013).
38. M. R. Lukatskaya et al., *Adv. Energy Mater.*, **5**, 1500589 (2015).
39. J. Come et al., *J. Electrochem. Soc.*, **159**, A1368 (2012).
40. Y. Dall'Agnese, P. Rozier, P.-L. Taberna, Y. Gogotsi, and P. Simon, *J. Power Sources*, **306**, 510 (2016).
41. M.-Q. Zhao et al., *Adv. Mater.*, **27**, 339 (2015).
42. M. Naguib et al., *ACS Nano*, **6**, 1322 (2012).
43. A. J. Higginson, thesis, *University of the Witwatersrand*, Johannesburg, South Africa (2011) http://wiredspace.wits.ac.za/handle/10539/10582.
44. K. Makgopa et al., *J. Mater. Chem. A*, **3**, 3480 (2015).
45. B. E. Conway, *Electrochemical Supercapacitors: Scientific Fundamentals and Technological Applications*, p. 734, Springer, (1999).
46. M. D. Stoller and R. S. Ruoff, *Energy Environ. Sci.*, **3**, 1294 (2010).
47. Z. Zhang et al., *J. Eur. Ceram. Soc.*, **37**, 43 (2017).
48. J. Frodelius et al., *Surf. Coat. Technol.*, **202**, 5976 (2008).
49. M. Sonestedt et al., *J. Mater. Sci.*, **45**, 2760 (2010).
50. W. K. Pang et al., *J. Alloys Compd.*, **509**, 172 (2011).
51. S. Rech et al., *Vacuum*, **94**, 69 (2013).
52. C. Li, S. Kota, C. Hu, and M. W. Barsoum, *J. Ceram. Sci. Technol.*, **7**, 301 (2016).
53. J. Li, Y. Du, C. Huo, S. Wang, and C. Cui, *Ceram. Int.*, **41**, 2631 (2015).
54. J. X. Li, Y. L. Du, and C. Cui, *Mater. Sci. Forum*, **833**, 44 (2015).
55. O. Mashtalir, M. Naguib, B. Dyatkin, Y. Gogotsi, and M. W. Barsoum, *Mater. Chem. Phys.*, **139**, 147 (2013).
56. O. Mashtalir et al., *Nat. Commun.*, **4**, 1716 (2013).
57. S. B. Yoon et al., *J. Am. Chem. Soc.*, **127**, 4188 (2005).
58. A. Nieto-Márquez, R. Romero, A. Romero, and J. L. Valverde, *J. Mater. Chem.*, **21**, 1664 (2011).
59. J. Wang, Y. Zhou, Z. Lin, F. Meng, and F. Li, *Appl. Phys. Lett.*, **86**, 101902 (2005).
60. J. Xie, X. Wang, A. Li, F. Li, and Y. Zhou, *Corros. Sci.*, **60**, 129 (2012).
61. V. Presser et al., *J. Raman Spectrosc.*, **43**, 168 (2012).
62. O. D. Leaffer, S. Gupta, M. W. Barsoum, and J. E. Spanier, *J. Mater. Res.*, **22**, 2651 (2007).
63. V. Presser et al., *J. Raman Spectrosc.*, **44**, 1060 (2013).
64. S. Lai et al., *Nanoscale*, **7**, 19390 (2015).
65. K. J. Cai, Y. Zheng, P. Shen, and S. Y. Chen, *CrystEngComm*, **16**, 5466 (2014).
66. A. C. Ferrari and J. Robertson, *Philos. Trans. R. Soc. Lond. Math. Phys. Eng. Sci.*, **362**, 2477 (2004).
67. A. C. Ferrari, *Solid State Commun.*, **143**, 47 (2007).
68. H. Qian et al., *Carbon*, **42**, 761 (2004).
69. M. D. Levi et al., *Adv. Energy Mater.*, **5**, 1400815 (2015).
70. M. Xu, L. Kong, W. Zhou, and H. Li, *J. Phys. Chem. C*, **111**, 19141 (2007).
71. V. Subramanian, H. Zhu, R. Vajtai, P. M. Ajayan, and B. Wei, *J. Phys. Chem. B*, **109**, 20207 (2005).
72. K. Fic, G. Lota, M. Meller, and E. Frackowiak, *Energy Environ. Sci.*, **5**, 5842 (2012).
73. P. Srimuk et al., *J. Mater. Chem. A*, **4**, 18265 (2016).
74. L. Hu et al., *Proc. Natl. Acad. Sci.*, **106**, 21490 (2009).
75. C. Wan, L. Yuan, and H. Shen, *Int J Electrochem Sci*, **9**, 4024 (2014).
76. Z. Fan et al., *Adv. Funct. Mater.*, **21**, 2366 (2011).
77. T. N. Y. Khawula, K. Raju, P. J. Franklyn, I. Sigalas, and K. I. Ozoemena, *J. Electrochem. Soc.*, **163**, A1927 (2016).
78. T. N. Y. Khawula, K. Raju, P. J. Franklyn, I. Sigalas, and K. I. Ozoemena, *J. Mater. Chem. A*, **4**, 6411 (2016).
79. K. Makgopa, K. Raju, P. M. Ejikeme, and K. I. Ozoemena, *Carbon*, **117**, 20 (2017).
80. S. A. Shah et al., *Chem. Commun.*, **53**, 400 (2017).
81. S. Yamamoto et al., *J. Phys. Condens. Matter*, **20**, 184025 (2008).
82. U. Diebold and T. E. Madey, *Surf. Sci. Spectra*, **4**, 227 (1996).
83. J. Halim et al., *Appl. Surf. Sci.*, **362**, 406 (2016).
84. Y. Wang et al., *J. Power Sources*, **327**, 221 (2016).
85. Y. Tong et al., *Appl. Surf. Sci.*, **434**, 283 (2018).
86. Y. Dall'Agnese et al., *Electrochem. Commun.*, **48**, 118 (2014).
87. M. P. Bichat, E. Raymundo-Piñero, and F. Béguin, *Carbon*, **48**, 4351 (2010).
88. D. Weingarth, A. Foelske-Schmitz, and R. Kötz, *J. Power Sources*, **225**, 84 (2013).
89. I. S. Ike, I. Sigalas, and S. E. Iyuke, *Phys. Chem. Chem. Phys.*, **18**, 28626 (2016).